

SUPPORTING INFORMATION

Controlled Kinetics of On-Surface Dehydrogenation using a Low-Energy Electron Beam

Anton Makoveev,¹ Pavel Procházka,¹ Azin Shasavar,¹ Lukáš Kormoš,¹ Tomáš Krajňák,¹

Veronika Stará,¹ and Jan Čechal^{1,2}*

¹CEITEC – Central European Institute of Technology, Brno University of Technology,
Purkyňova 123, 612 00 Brno, Czech Republic.

³Institute of Physical Engineering, Brno University of Technology, Technická 2896/2, 616 69
Brno, Czech Republic.

CONTENTS:

1. Analysis of the ε phase on Ag(001)
2. The fully deprotonated phase on Ag(111)
3. Diffraction analysis of e-beam induced transformation at Ag (0001)
4. Reaction rate from the α to α' phase transformation
5. Intensity change in the bright field as a function of electron energy
6. DFT calculations: work function change upon deprotonation
7. Electron reflectivity as a function of deprotonation fraction
8. Details of fitting of the XPS data
9. Water adsorption at 90 K
10. DFT calculations: O-H dissociation
11. References

1. Analysis of the ϵ phase on Ag(001)

XPS analysis of the ϵ phase on Ag(001) and its comparison with the thermally obtained δ phase is given in Figure S1.1. The XPS analysis, including peak fitting, was performed consistently with our preceding works.^{1,2} Both spectra show only one peak associated with deprotonated molecules. As there are negligible differences between them, as given in Tables S1.1 and S1.2, we conclude that the ϵ phase comprises only the fully deprotonated BDA molecules.

Figure S1.2 shows LEEM bright- and dark-field images and diffraction patterns and unit-cell model of the ϵ phase. The simulated diffraction patterns given in Figure S1.2g based on the model presented in Figure S1.2h are consistent with measured diffraction patterns. The associated unit cell in matrix notation is $\begin{pmatrix} 3 & -2 \\ 3 & 2 \end{pmatrix}$; there are two symmetry equivalent domains of the ϵ phase with respect to Ag(001) substrate. The proposed unit cell shows a good match with the real-space STM image given in Figure S1.3. STM also reveals that the domains of the ϵ phase are limited in size to max. 10 – 15 molecules in both directions. This suggests that there is a build-up of stress with increasing domain size. The stress is relaxed by a different structure on the domain perimeters, which resembles the thermally obtained δ phase. The annealing of the ϵ phase to 310 K results in its fast transformation to the δ phase.

Table S1.1: Peak-fit parameters: binding energy position (BE) and FWHM of the Gaussian part of the C 1s peak components. Lorentzian width is 0.3 eV. The BE shifts (from the peak, marked +0.0) are given in brackets.

	Component C1 (phenyl ring)		Component C2 (phenyl ring)		Component C3 (carboxyl)		Component C4 ($\pi - \pi^*$)	
	BE (eV)	FWHM (eV)	BE (eV)	FWHM (eV)	BE (eV)	FWHM (eV)	BE (eV)	FWHM (eV)
ϵ	284.50 (+0.0)	1.0	285.5 (+1.0)	1.0	287.9 (+3.2)	1.5	291.6 (+7.1)	2.3
δ	284.50 (+0.0)	1.0	285.5 (+1.0)	1.0	287.9 (+3.2)	1.5	291.5 (+7.0)	2.0

Table S1.2: Peak-fit parameters: binding energy position (BE) and FWHM of the Gaussian part of the O 1s peak components. Lorentzian width is 0.1 eV.

	Component O1 (carboxylate oxygen)	
	BE (eV)	FWHM (eV)
ϵ	530.62	1.35
δ	530.57	1.30

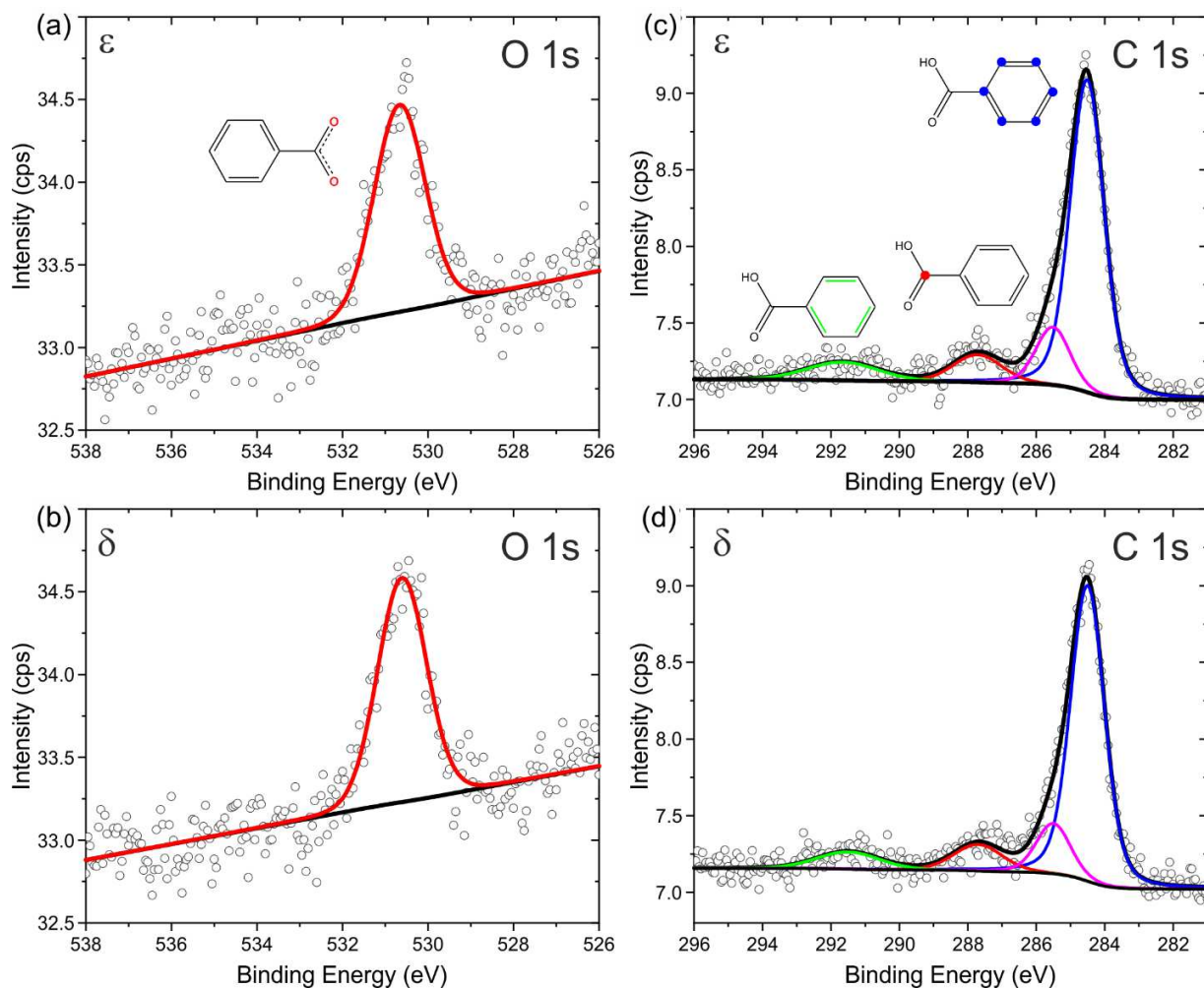


Figure S1.1: Detailed spectra of O 1s (left) and C 1s (right) measured on samples with the ϵ (e-beam induced) and δ (thermally induced) phases.

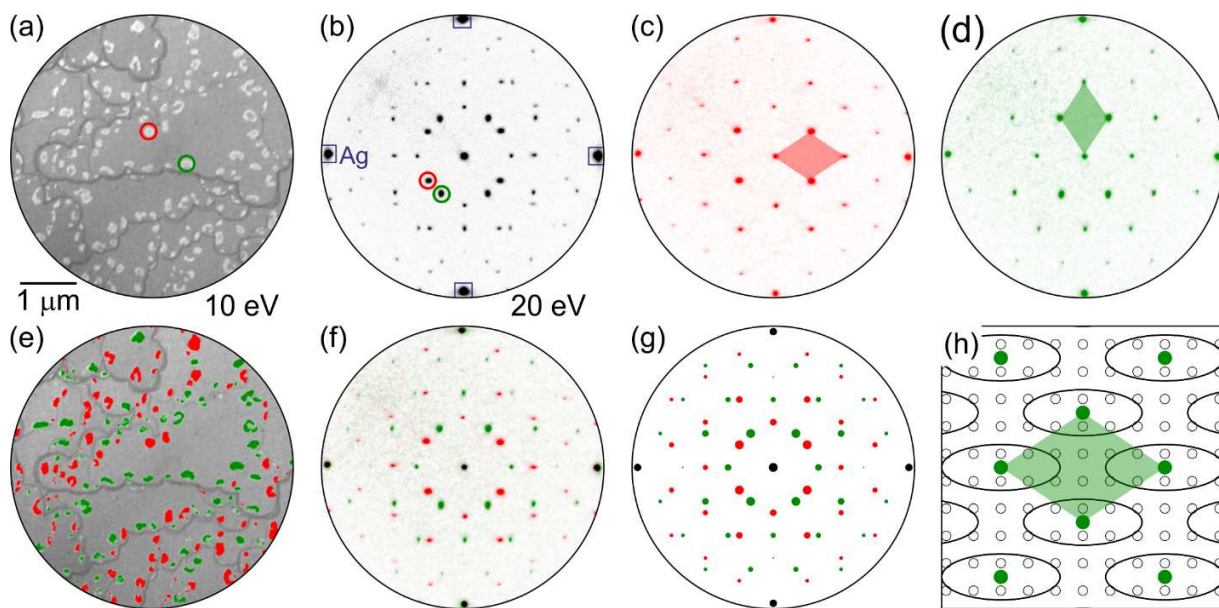


Figure S1.2: LEEM analysis of Ag(001) substrate with sub-monolayer coverage of the ϵ phase. (a) Bright-field image collected at 10 eV. Molecular islands appear as bright areas on the dark substrate. (b) Corresponding diffraction pattern taken at 20 eV. Blue squares mark the substrate spots. (c) and (d) μ -diffraction patterns collected from individual ϵ phase domains measured at encircled positions in (a). Red and green rhombi represent reciprocal unit cells of the ϵ phase. (e) Color-coded composition of dark-field images obtained by real-space projection of diffraction spots highlighted in (b). (f) Color-coded composition of μ -diffraction patterns shown in (c) and (d). (g) Simulated diffraction pattern for real-space unit cell model given in (h).

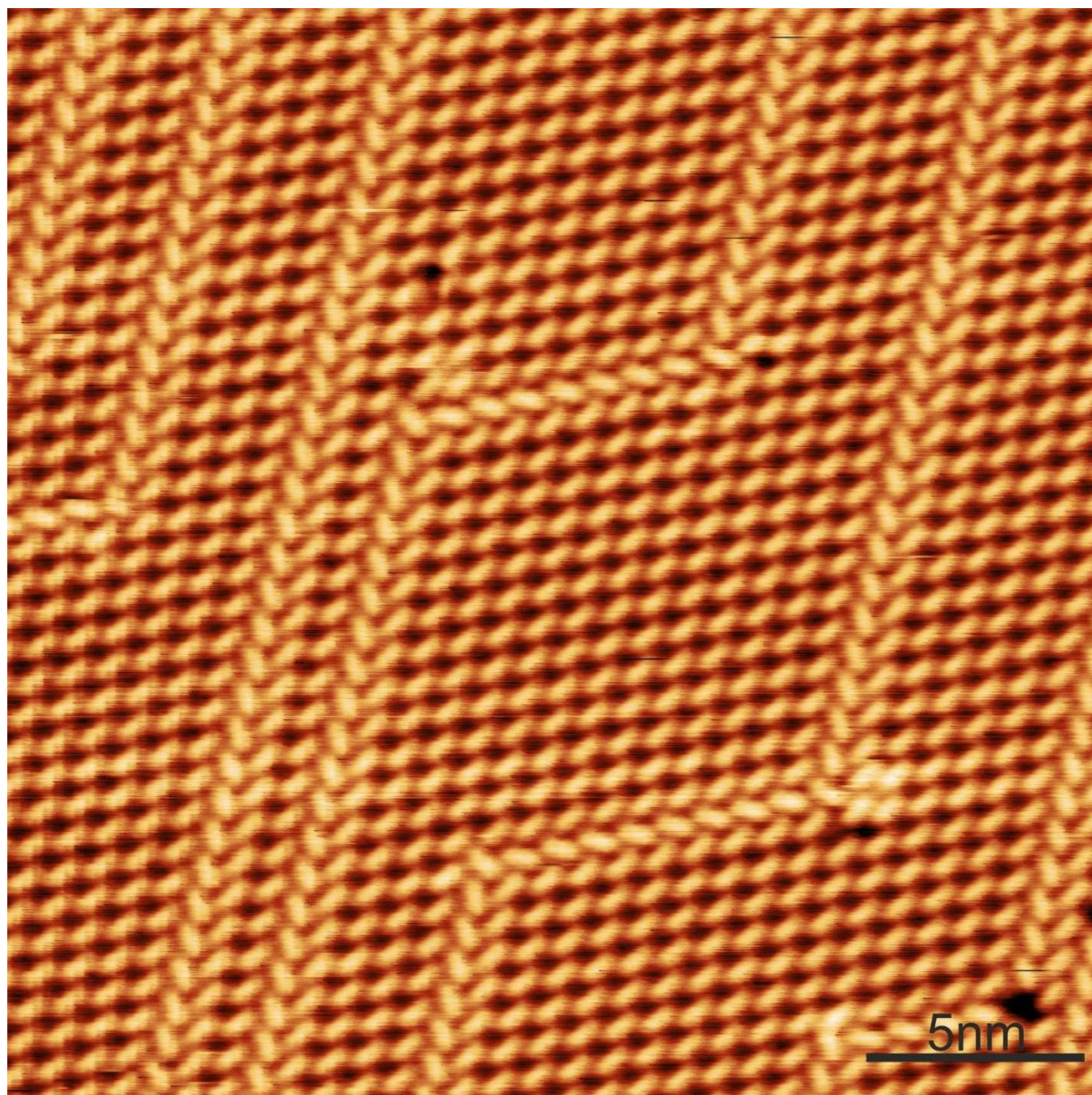


Figure S1.3: STM image of the ϵ phase at Ag(001). The ϵ phase forms size-limited domains surrounded by stripes of differently arranged molecules. The molecular structure within the stripes resembles the δ phase. Acquisition parameters: $V_{\text{sample}} = -60$ mV, $I = 60$ pA, room temperature.

2. The fully deprotonated phase on Ag(111)

The fully deprotonated phase on the Ag(111) substrate has a structure similar to the δ phase on Ag(001)² as documented by the single domain diffraction pattern given in Figure S2.1a and STM image in Figure S2.1b. Our forthcoming paper on the full description of BDA phases on Ag(111) provides a thorough description of this phase.

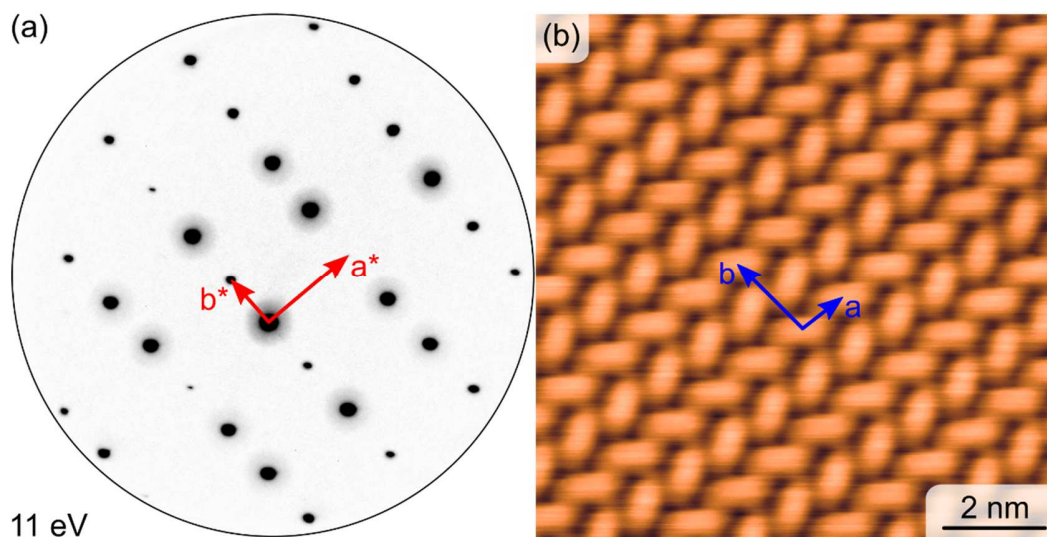


Figure S2.1: (a) μ -diffraction and (b) STM of the BDA δ phase on Ag(111). The red and blue arrows represent the reciprocal and real unit cell vectors, respectively.

3. Diffraction analysis of e-beam induced transformation at Ag (100)

Figure S3.1 shows an evolution of the intensity of diffraction spots associated with the ε phase as a function of electron beam energy; this figure is an analog for Figure 3 in the main text but Ag(001) substrate. However, at Ag(001), the electron beam with energy ≤ 10 eV first induces the formation of the β phase, which largely influences the formation of the ε phase for these energies. Hence, the data points for energies ≤ 10 eV should not be considered as a reliable measure for e-beam deprotonation kinetics.

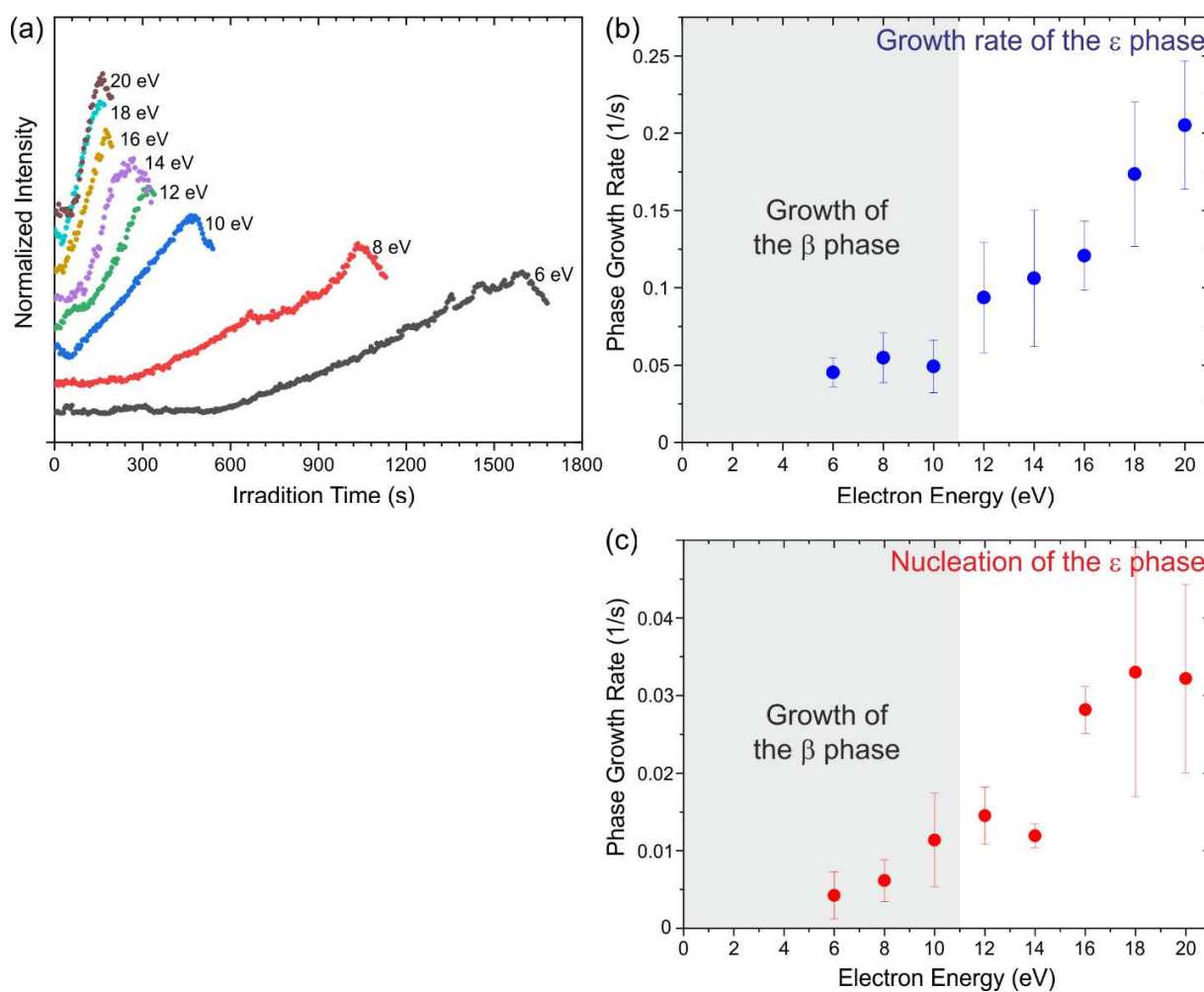


Figure S3.1: (a) Time evolution of the intensity of diffraction spots associated with the ε phase on Ag(100) for the energy of incident electron beam 6 – 20 eV. (b, c) The ε phase nucleation rate as a function of e-beam energy determined from (b) growth of intensity of diffraction spot and (c) inverse time necessary to nucleate the ε phase. Energies at which the intermediate β phase grows at highlighted by a gray background.

4. Reaction rate from the α to $\dot{\alpha}$ phase transformation

The intensity of the diffraction spots associated with $\dot{\alpha}$ phase gradually increases upon the e-beam irradiation and reaches the maximum at a specific time (Figure S4.1).

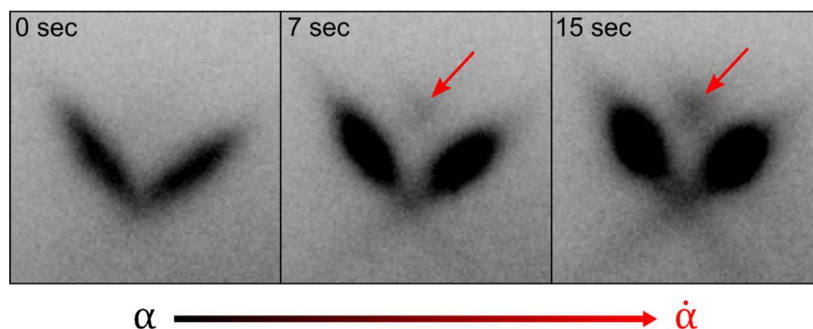


Figure S4.1: Time-dependent formation and intensity change of a diffraction spot associated with the $\dot{\alpha}$ phase upon e-beam irradiation at 12 eV. The red arrows indicate an emerging $\dot{\alpha}$ phase diffraction spot. The contrast is inverted for clarity.

To determine the rate of the intensity change, we have measured the time evolution of the average intensity of pixels within a rectangle around the $\dot{\alpha}$ diffraction spot (Figure S4.2). The rate is then proportional to the inverse time necessary to reach the maximum intensity ($1/t_{\max}$). This parameter is depicted in Figure 5g of the main text as a function of the e-beam energy.

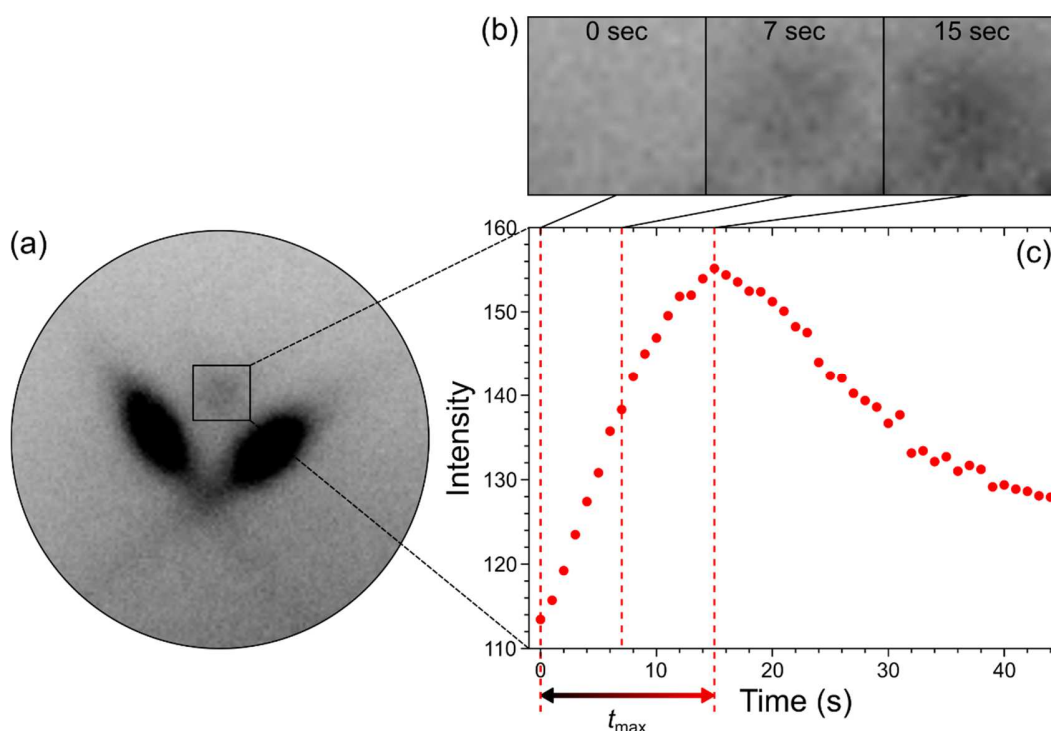


Figure S4.2: Time evolution of the intensity associated with the α diffraction spot. The rectangle in (a) indicates the area from which the average intensity of pixels has been measured in time; the example of three frames is given in (b). (c) The average intensity of the frames as a function of time. The contrast in all images is inverted.

5. Intensity change in the bright field as a function of electron energy

We have used the following experimental procedure to measure the time evolution of the BDA reflected e-beam intensity (intensity in following) in the real-space LEEM images. (i) First, we have irradiated a small area with 30-eV electrons for 500 s through an aperture diameter of $3.7\ \mu\text{m}$ (dark area in Figure S5.1a). The intensity of BDA islands within this area serves as a reference point for the fully deprotonated state. (ii) After the pre-irradiation, we have closed a valve between the sample and electron source, removed the aperture, changed the e-beam energy to the desired one, and opened the valve again. (iii) Then, the intensity was recorded in time at the chosen energy for 500 s. The initial intensity of BDA islands outside the pre-irradiated area serves as the reference point for non-deprotonated BDA islands. Hence, we have two reference points for the normalization of the measured intensity to the deprotonation.

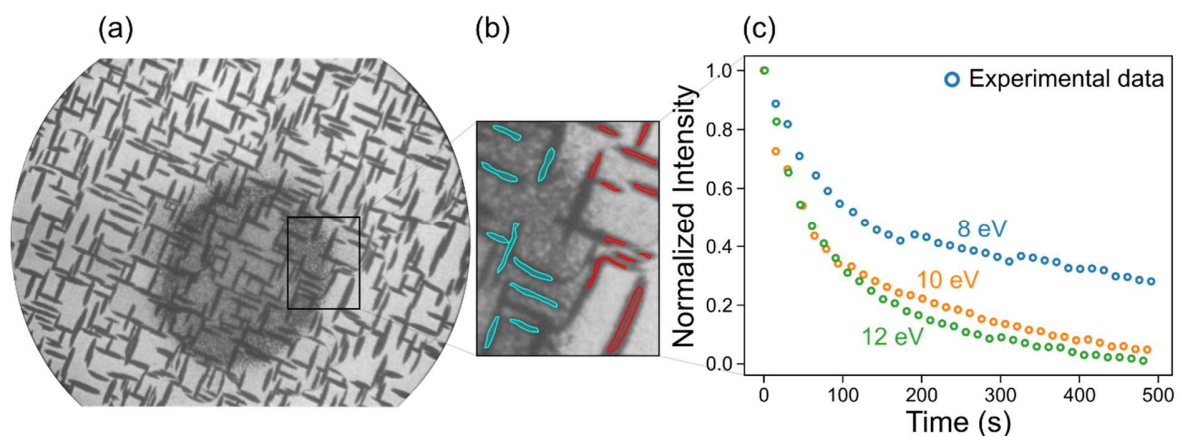


Figure S5.1: (a) A LEEM bright-field image with $10\ \mu\text{m}$ view field. The central dark area represents the region pre-irradiated with a 30-eV e-beam for 500 seconds. The black rectangle highlights the place where the intensity data have been collected and processed. (b) A magnified rectangular area from (a). The intact and pre-irradiated BDA islands used for contrast measurement are highlighted in red and cyan, respectively. (c) The temporal evolution of the intensity of the islands highlighted red in (b).

The recorded video sequences were evaluated, and the time evolution of normalized intensities was used for further processing. To minimize unwanted effects related to inhomogeneity of the LEEM detector, we have measured average intensities of pixels associated with the intact and irradiated BDA molecules (marked by red and cyan in Figure S5.1b) in a small

rectangular region at the border between pre-irradiated and surrounding areas (Figure S5.1a, b). The time evolution of normalized intensity for selected energies is given in Figure S41c.

To model the measured data, we assume that (i) the probability of deprotonation of BDA carboxyl groups is independent of the deprotonation state of the system and (ii) the measured intensity linearly depends on the fraction of deprotonated carboxyl groups. Both these assumptions are discussed in Section 6 of this Supporting Information. If these assumptions are valid, the temporal evolution of the fraction of deprotonated molecules follows the first-order kinetics. For the first-order kinetics, the change in the amount of fully protonated BDA molecules can be expressed as $\frac{d[C_{\text{COOH}}]}{dt} = -k[C_{\text{COOH}}]$, where C_{COOH} is the concentration of fully protonated BDA, and k the reaction rate constant. Integrating this expression leads exponential decrease in the concentration of the protonated groups, i.e., $C_{\text{COOH}} \sim \exp(-kt)$. The slope of linear fitting of the logarithm of the intensity data with respect to time gives the negative deprotonation rate, $-k$, presented in Figure S5.2. Here, only the initial 10 % intensity drop was considered to ensure the validity of (ii).

Whereas the obtained deprotonation rates resemble those obtained by diffraction up to 12 eV of energy, we note that our calibration measurements given in Section 6 of this Supplementary Discussion show that the intensity should increase with deprotonation. This behavior indicates the presence of another phenomenon than deprotonation, which influences the formation of the BDA LEEM contrast under the e-beam irradiation. The possible reason could be defocusing due to the electric field created by charge collecting at BDA molecules that alter electron trajectories.³ If one wants to get the information exclusively on the deprotonation reaction from real-space LEEM measurements, it is necessary to distinguish and compensate for the additional contrast mechanism.

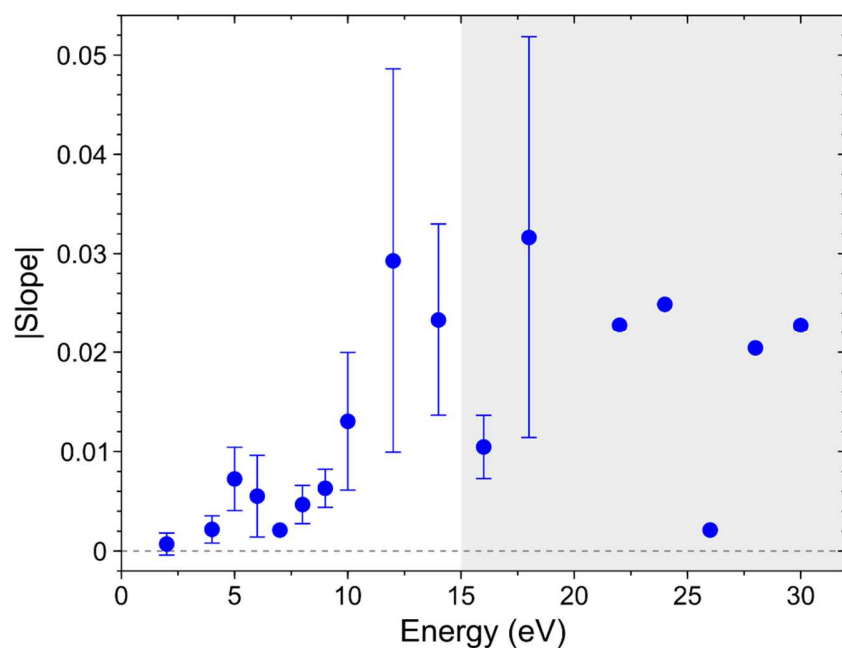


Figure S5.2: The absolute values of the linear fitting slopes corresponding to the deprotonation rate constants for the initial 10 % of the intensity drop (see text for explanation) at different energies. The error bars indicate one standard deviation. The shaded area highlights the e-beam energies, at which the contrast change is very small or even reversed.

6. DFT calculations: work function change upon deprotonation

Global energy minimizations were carried out using the density functional theory (DFT) using the Vienna Ab-initio Simulation Package (VASP).⁴⁻⁷ Projector augmented wave (PAW) pseudopotential^{8,9} and Perdew-Burke-Ernzerhof (PBE)^{10,11} exchange-correlation functional were used to study the self-assembled monolayer consisting of four BDA molecules on 4 silver atomic layers. The plane wave cut-off energy was set to 400 eV, and Γ point calculation was used for preliminary calculations. For final optimization, we have used a 3×3 Monkhorst and Pack scheme, which gives well-converged results for the large unit cells.^{12,13}

Fully protonated BDAs are considered for the α phase. The $\dot{\alpha}$ phase was simulated by cleaving hydrogen off a carboxylic group, as detailed in our previous work.¹⁴ The work function corresponds to the energy of extracting an electron from the Fermi level to the vacuum level in infinity. Regarding surface work function (φ), it is generally considered that there are two main effects inducing changes in the work function: charge transfer and push-back effect. Herein, charge flow from adsorbents to the substrate implies decreasing the φ and vice versa.¹⁵⁻¹⁸ Concerning the push-back (pillow) effect,^{12,22-26} the electron spill out from metal will push back through the adsorption because of the electron density of the adsorbents so the interface dipole and consequently the work function will decrease. In our recent report,¹⁴ we have observed electron transfer from the substrate to BDA upon the transition from the α to $\dot{\alpha}$ phase. Hence, a higher φ for $\dot{\alpha}$ phase is expected. However, to be more precise, dipole correction calculations along periodic slabs were adopted to avoid false interactions caused by interface dipole and consider the push-back effect. Upon BDA adsorption, the work function lowers by 0.07 eV compared to the clean Ag(001), and when one hydrogen was removed, the work function further reduces by 0.22 eV (0.29 eV compared to the Ag substrate). As a result, the work function is decreasing across phase growth/changes, $\varphi_{\text{Ag}(100)} > \varphi_{\alpha} > \varphi_{\dot{\alpha}}$. These changes are dominated by push-back effect with a minor contribution of formed interface dipole. The work function reduction due to growth on the metal surfaces aligns with the previous theoretical and experimental reports.^{12,15,19-21} It is worth mentioning our complementary results for work function changes for BDA on a different substrate, Ag(111), are consistent with those by Heintz *et al.*¹³ who reported an increase in φ for terephthalic acid (TPA) monolayer adsorbed on Ag(111).

7. Electron reflectivity as a function of deprotonation fraction

To reveal the dependence of real-space BDA intensity on its deprotonation state, we have performed step-by-step thermal deprotonation, corresponding to the α to $\dot{\alpha}$ transformation of a full BDA layer with LEEM and XPS characterization in between. The experiment was conducted in the following way. (i) Employing XPS of the deprotonation state of the sample has been measured. (ii) Afterwards, the sample was transferred to the LEEM, where the intensity associated with the BDA layer was measured in the range of 3 – 30 eV with the step of 1 eV. For each e-beam energy, we have measured the intensity at 8 distinct places to obtain good statistics. All the intensities were measured right after opening the primary beam stopper to prevent undesirable changes in the intensity due to the impact of the electron beam on BDA. (iii) Then, the sample was annealed to induce further deprotonation closing the complete measurement cycle. To collect the necessary amount of experimental data points, we repeated the cycle (i) – (iii) a few times (Figure S6a) until 50 % deprotonation had been reached. In this way, we have collected a set of so-called I(V) curves for several deprotonation states, as shown in Figure S7.1b.

The change in the intensity of the reflected electron beam is inherently connected with the change of the work function, one of the principal contrast mechanisms in LEEM. DFT calculations (Section 5 of this Supporting Information) show the 0.22 eV decrease in work function as a result of the change in the interface dipoles upon the deprotonation and stronger binding of carboxylate oxygens to the substrate. Hence the deprotonation and the α to $\dot{\alpha}$ transformation should be accompanied by the change of the contrast that can be followed in time by LEEM bright-field imaging. In further analysis, we have assumed that the probability of deprotonation of BDA's carboxylic groups is not influenced by the presence of the deprotonated group in its vicinity. This condition is fulfilled during the initial stages of deprotonation if the deprotonation occurs at random locations. Increasing the density of places with a distinct work function results in a gradual change in the measured intensity. Hence, based on the assumption of independent deprotonation, we have supposed a linear behavior of the measured intensity as a function of the deprotonation. Consistently with our hypothesis, the linear behavior was found only for deprotonation fractions up to 22 % (see the inset of Figure S7.1c).

The magnitude of intensity change with deprotonation, i.e., the slopes obtained by the linear fitting, are shown in Figure S7.1c as a function of the e-beam energy. The magnitude of change is the largest for e-beam energy 5 eV, at which a distinct feature appears on the I(V) curve.

The slope becomes close to zero, having both positive and negative values for energies > 14 eV; hence, for these energies, the sensitivity for deprotonation is low. Importantly, for energies up to 14 eV, the slope is positive, meaning that the reflected electron intensity increases with deprotonation (deprotonated BDA islands become brighter than non-deprotonated). However, during the e-beam irradiation, we observed a decrease in intensity; therefore, the time evolution does not reflect the deprotonation itself, and a different mechanism is responsible for the change.

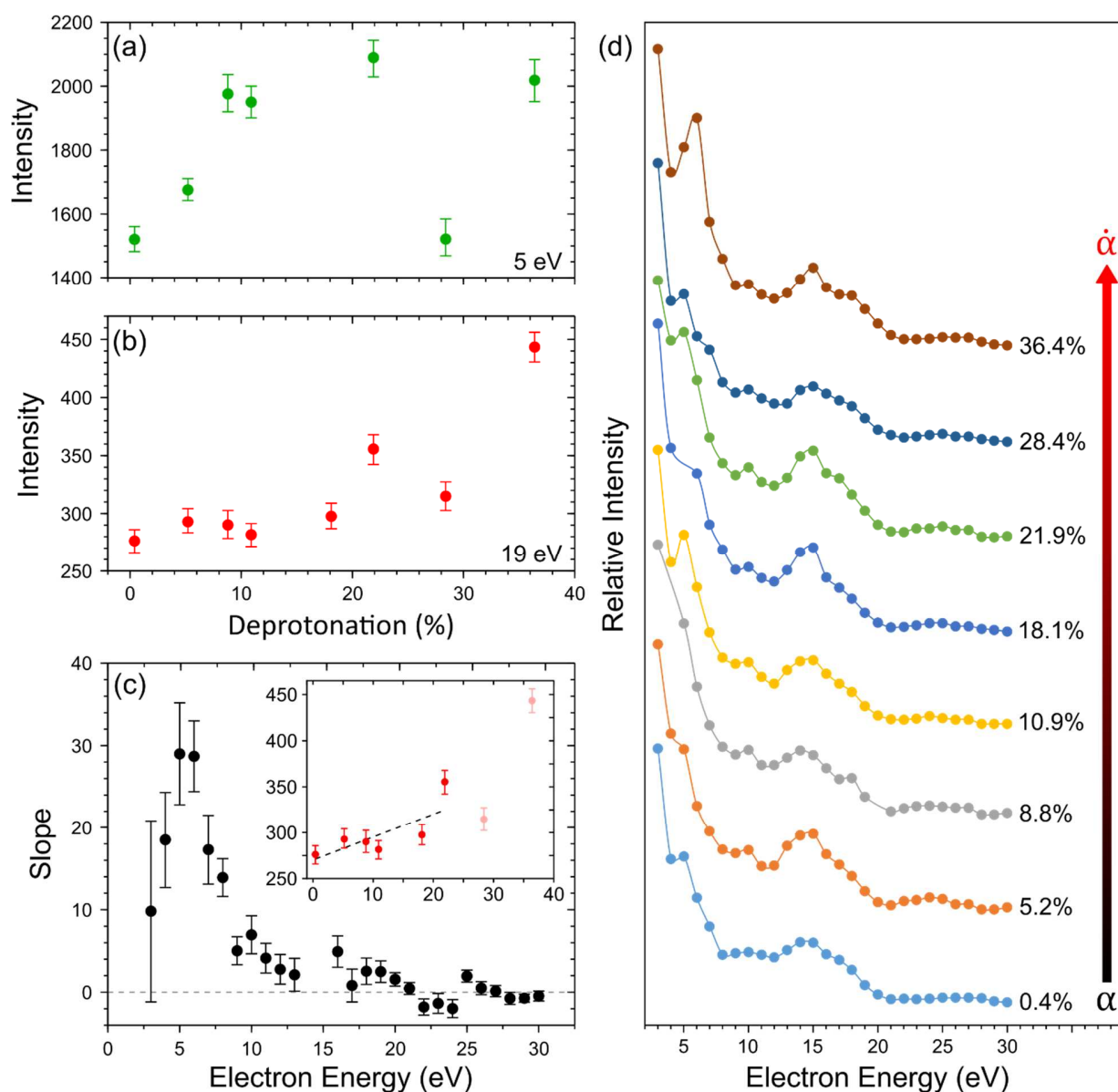


Figure S7.1: (a) and (b) The dependence of real-space BDA intensity on the fraction of deprotonated carboxyl groups at e-beam energy of 5 eV and 19 eV, respectively. The experimental points represent medians, and the error bars indicate an interquartile range. (c) The slopes of linear

expressions fitted to the first six deprotonation states (an example for 19 eV is given in the inset) for different e-beam energies. Based on the chi-square test, the linear fits are consistent with the experimental data with a probability of 95 %. The error bars indicate the standard error. (d) I(V) curves for the deprotonation fractions specified on the right.

8. Details of fitting of the XPS data

X-ray-induced deprotonation was followed in real-time by XPS on samples cooled to the measurement temperature. For the analysis, we have employed a combination of models used for fitting the α and $\dot{\alpha}$ phases as described in refs. 1,14. The example of fitting and marking the peaks is given in Figure S8.1. The fraction of deprotonated molecules was determined as the intensity of the carboxylate peak in the $\dot{\alpha}$ phase ($O_{\dot{\alpha}}^1$) to the total intensity of peak, i.e., $f_D = \frac{O_{\dot{\alpha}}^1}{O_{\dot{\alpha}}^1 + O_{\dot{\alpha}}^2 + O_{\dot{\alpha}}^3 + O_{\alpha}^1 + O_{\alpha}^2}$.

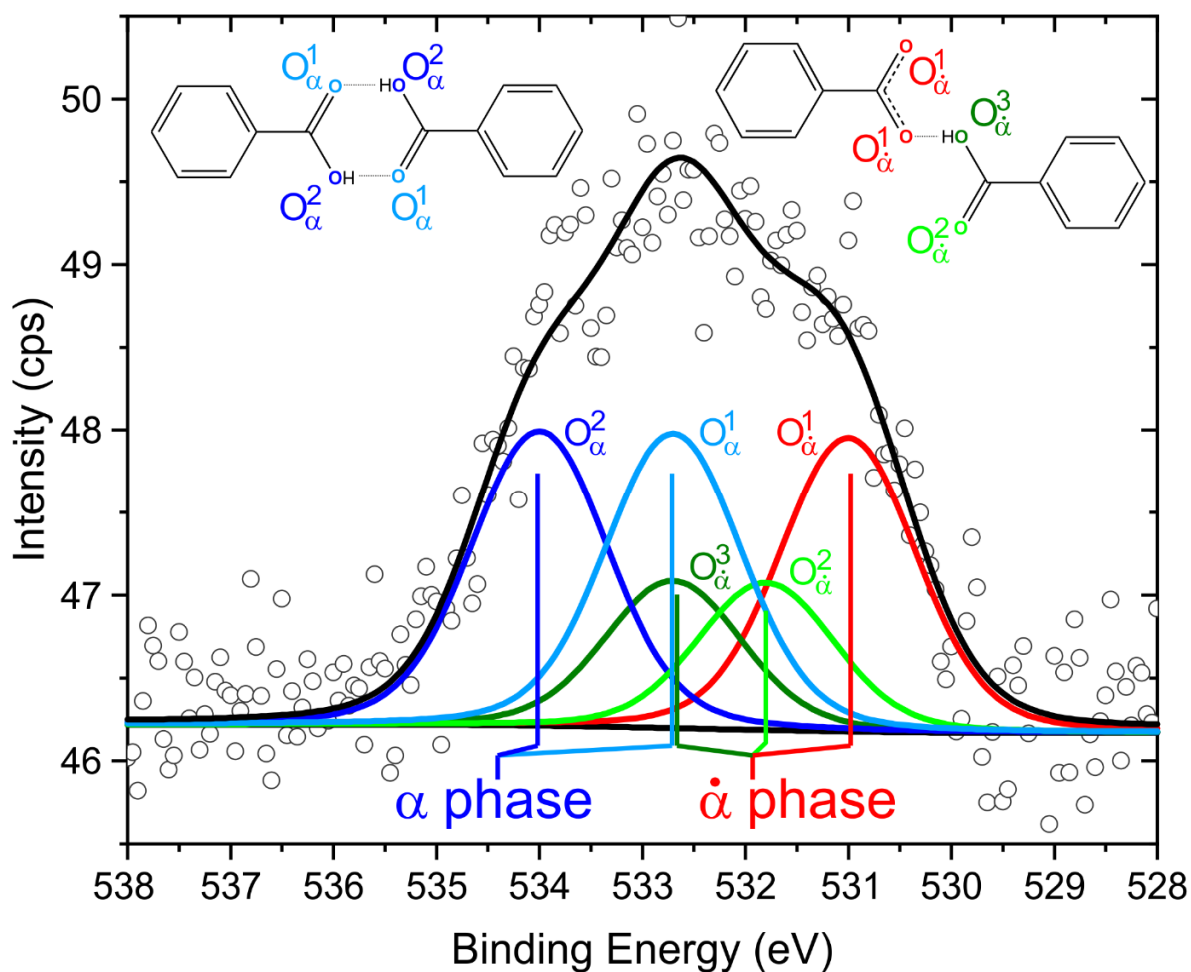


Figure S8.1: Fitting of XPS spectra measured after 1800 minutes of X-ray exposure. The fitting gives the fraction of deprotonated molecules of 0.25. The α phase is fitted by 2 components with equal intensity associated with hydroxyl and carbonyl oxygens (O_{α}^2 : blue and O_{α}^1 : light blue, respectively). The $\dot{\alpha}$ phase is described by 3 components: hydroxyl and carbonyl oxygens of the carboxyl group ($O_{\dot{\alpha}}^3$: green and $O_{\dot{\alpha}}^2$: light green), which is bonded to carboxylate (two equal oxygens $O_{\dot{\alpha}}^1$: red).

9. Water adsorption at 90 K

During the measurement of the time series at 90 K, we have observed a linear increase in O 1s intensity; this excess oxygen disappears at 140 K (Figure S9.1). We associate the changes with the adsorption of water at the surface, which desorbs at 140 K.

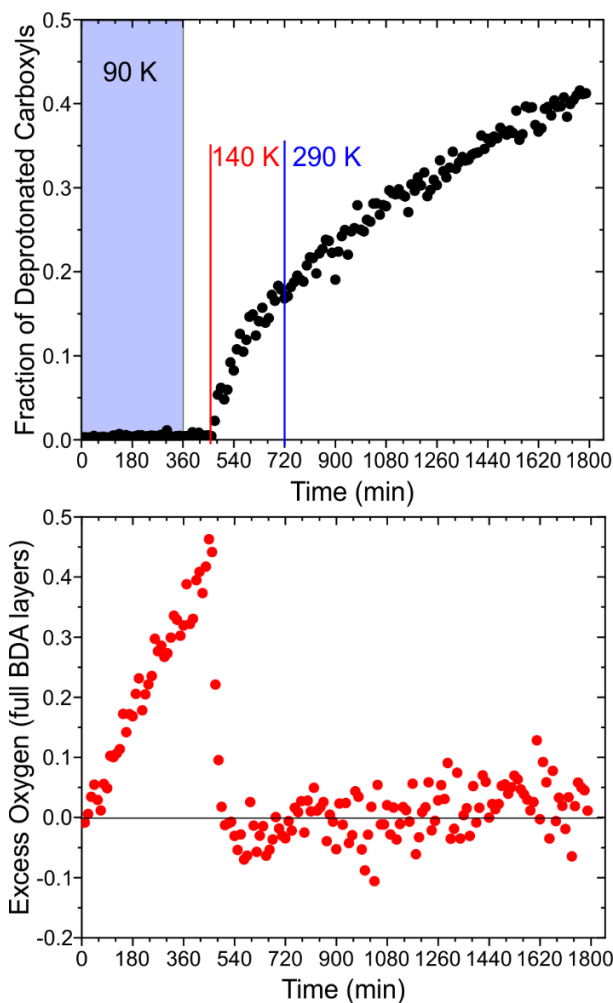


Figure S9.1: (top) Time evolution of the fraction of deprotonated molecules. The blue-colored region marks cooling to 90 K. (bottom) Time evolution of the total intensity of O 1s peak.

10. DFT calculations: O-H dissociation

To get a deeper insight into the multistep deprotonation reaction carboxyl groups, we have performed extended DFT calculations detailed in Section 6 of this Supplementary Information. Deprotonation starts with the O–H bond dissociation; the discussed hydrogen is highlighted by blue color in Figure S10.1a. Subsequently, the parent oxygen binds with the substrate silver atom, and the hydrogen is associatively desorbed, as depicted in Figure S10.1d. We have found a metastable configuration associated with a local energy minimum along the reaction coordinate. In this configuration, the oxygen atom O4 is bound to the substrate, and the hydrogen remains bound to its parent oxygen (O4), as presented in Figure S10.1b. We have found that this configuration is slightly favorable in respect to the original configuration (the α phase). The hydrogen (H4) still considerably interacts with its parent oxygen; the d_{O4-H4} distance is still ~ 1.0 Å. We note that in this configuration, the O1–H1 \cdots O3 hydrogen bond is weaker as compared to the α phase. The strong low barrier hydrogen bond in α phase ($d_{O1-H1} \approx d_{H1-O3} \approx 1.1$ Å)¹⁴, turns to a moderate with $d_{O1-H1} = 1.0$ and $d_{H1\cdots O3} = 1.6$ Å.

To assess the stability of the H4 atom in the metastable configuration, we have calculated enthalpies given in Figure 7 of the main text associated with configurations given in Figure S10.1. We have considered the 2×2 BDA unit cell of the α phase as a suitable reference. The direct comparison between the α and α phase renders the latter seemingly energetically unfavorable by 0.4 eV. However, the discussed hydrogen is missing in the reference α phase. Considering its associative desorption, the total enthalpy gain for the deprotonation reaction and the α phase formation is 0.3 eV. Moreover, there is ~ 0.5 eV entropy gain associated with associative hydrogen desorption at our experimental conditions.²⁷ Hence the dehydrogenation reaction is both exothermic and exergonic, in which the release of hydrogen plays a dominant role.

However, there is a significant activation barrier associated with hydrogen desorption. First, the H atom has to diffuse out of the metastable position shown in Figure S10.1b and associatively desorb with another hydrogen atom. We estimate the barrier height as a difference between the enthalpy in the transition state and the metastable position. To estimate the energy in the transition state, we considered two configurations: the reference α phase and the unrealistic scenario of direct removal of the H atom from the surface along the surface normal. The first

configuration gives an activation barrier height of 0.5 eV, whereas the latter gives 0.6 eV and presents a reasonable estimate for the maximum barrier height.

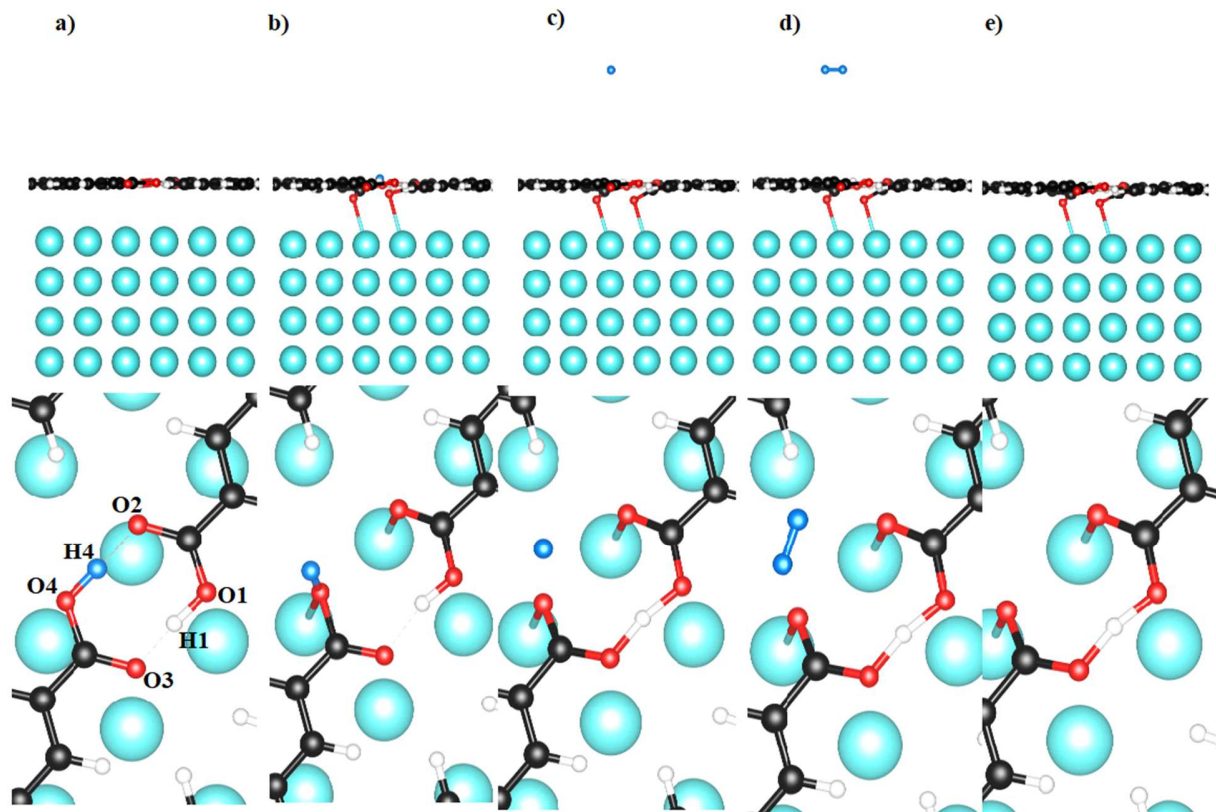


Figure S10.1: Side and top views of optimized geometry to assess the energetics of the deprotonation reaction. (a) α phase; (b) α phase with a hydrogen atom in the vicinity of its parent oxygen; (c) α phase with hydrogen atom artificially moved outside the surface (d) α and a free hydrogen molecule, and (e) reference α phase. Cyan, black, red, and white spheres represent Ag, C, O, and H atoms. The discussed oxygen is given in blue for clarity.

11. References

- (1) Procházka, P.; Procházka, P.; Gosálvez, M. A.; Gosálvez, M. A.; Gosálvez, M. A.; Kormoš, L.; De La Torre, B.; De La Torre, B.; Gallardo, A.; Gallardo, A.; et al. Multiscale Analysis of Phase Transformations in Self-Assembled Layers of 4,4'-Biphenyl Dicarboxylic Acid on the Ag(001) Surface. *ACS Nano* **2020**, *14*, 7269–7279.
- (2) Kormoš, L.; Procházka, P.; Makoveev, A. O.; Čechal, J. Complex K-Uniform Tilings by a Simple Bitopic Precursor Self-Assembled on Ag(001) Surface. *Nat. Commun.* **2020**, *11*, 1856.
- (4) Kresse, G.; Furthmüller, J. Efficiency of Ab-Initio Total Energy Calculations for Metals and Semiconductors Using a Plane-Wave Basis Set. *Comput. Mater. Sci.* **1996**, *6*, 15–50.
- (5) Kresse, G.; Furthmüller, J. Efficient Iterative Schemes for Ab Initio Total-Energy Calculations Using a Plane-Wave Basis Set. *Phys. Rev. B* **1996**, *54*, 11169–11186.
- (6) Kresse, G.; Hafner, J. Ab Initio Molecular-Dynamics Simulation of the Liquid-Metal–Amorphous-Semiconductor Transition in Germanium. *Phys. Rev. B* **1994**, *49*, 14251–14269.
- (7) Kresse, G.; Hafner, J. Ab Initio Molecular Dynamics for Liquid Metals. *Phys. Rev. B* **1993**, *47*, 558–561.
- (8) Kresse, G.; Joubert, D. From Ultrasoft Pseudopotentials to the Projector Augmented-Wave Method. *Phys. Rev. B* **1999**, *59*, 1758–1775.
- (9) Blöchl, P. E. Projector Augmented-Wave Method. *Phys. Rev. B* **1994**, *50*, 17953–17979.
- (10) Perdew, J. P.; Burke, K.; Ernzerhof, M. Generalized Gradient Approximation Made Simple [Phys. Rev. Lett. 77, 3865 (1996)]. *Phys. Rev. Lett.* **1997**, *78*, 1396–1396.
- (11) Perdew, J. P.; Burke, K.; Ernzerhof, M. Generalized Gradient Approximation Made Simple. *Phys. Rev. Lett.* **1996**, *77*, 3865–3868.
- (12) Rusu, P. C.; Giovannetti, G.; Weijtens, C.; Coehoorn, R.; Brocks, G. First-Principles Study of the Dipole Layer Formation at Metal-Organic Interfaces. *Phys. Rev. B - Condens. Matter Mater. Phys.* **2010**, *81*, 1–17.
- (13) Heintz, J.; Durand, C.; Tang, H.; Coratger, R. Control of the Deprotonation of Terephthalic Acid Assemblies on Ag(111) Studied by DFT Calculations and Low Temperature Scanning Tunneling Microscopy. *Phys. Chem. Chem. Phys.* **2020**, *22*, 3173–3183.
- (14) Procházka, P.; Kormoš, L.; Shahsavari, A.; Stará, V.; Makoveev, A. O.; Skála, T.; Blatnik,

- M.; Čechal, J. Phase Transformations in a Complete Monolayer of 4,4'-Biphenyl-Dicarboxylic Acid on Ag(0 0 1). *Appl. Surf. Sci.* **2021**, *547*.
- (15) Michaelides, A.; Hu, P.; Lee, M. H.; Alavi, A.; King, D. A. Resolution of an Ancient Surface Science Anomaly: Work Function Change Induced by N Adsorption on [Formula Presented]. *Phys. Rev. Lett.* **2003**, *90*, 4. <https://doi.org/10.1103/PhysRevLett.90.246103>.
- (16) Mignolet, J. C. P. Studies in Contact Potentials. Part I.—The Adsorption of Some Gases on Evaporated Nickel Films. *Discuss. Faraday Soc.* **1950**, *8*, 105–114.
- (17) Attard, G.; Barnes, C. *Surfaces*; Oxford University Press, 1998.
- (18) Breedon, M.; Spencer, M. J. S.; Yarovsky, I. Adsorption of NO and NO₂ on the ZnO(2 over(1, 7) over(1, 7) 0) Surface: A DFT Study. *Surf. Sci.* **2009**, *603* (24), 3389–3399.
- (19) De Renzi, V.; Rousseau, R.; Marchetto, D.; Biagi, R.; Scandolo, S.; Del Pennino, U. Metal Work-Function Changes Induced by Organic Adsorbates: A Combined Experimental and Theoretical Study. *Phys. Rev. Lett.* **2005**, *95*, 046804.
- (20) Camino, B.; Noakes, T. C. Q.; Surman, M.; Seddon, E. A.; Harrison, N. M. Photoemission Simulation for Photocathode Design: Theory and Application to Copper and Silver Surfaces. *Comput. Mater. Sci.* **2016**, *122*, 331–340.
- (21) Chang, V.; Noakes, T. C. Q.; Harrison, N. M. Work Function and Quantum Efficiency Study of Metal Oxide Thin Films on Ag(100). *Phys. Rev. B* **2018**, *97*, 155436.
- (22) Kahn, A. Fermi Level, Work Function and Vacuum Level. *Mater. Horizons* **2016**, *3*, 7–10.
- (23) Otero, R.; Vázquez de Parga, A. L.; Gallego, J. M. Electronic, Structural and Chemical Effects of Charge-Transfer at Organic/Inorganic Interfaces. *Surf. Sci. Rep.* **2017**, *72*, 105–145.
- (24) de Silva, J. L. F.; Stampfl, C.; Scheffler, M. Adsorption of Xe Atoms on Metal Surfaces: New Insights from First-Principles Calculations. *Phys. Rev. Lett.* **2003**, *90* (6), 4.
- (25) Bagus, P. S.; Staemmler, V.; Wöll, C. Exchangeliike Effects for Closed-Shell Adsorbates: Interface Dipole and Work Function. *Phys. Rev. Lett.* **2002**, *89*, 096104.
- (26) Witte, G.; Lukas, S.; Bagus, P. S.; Wöll, C. Vacuum Level Alignment at Organic/Metal Junctions: “Cushion” Effect and the Interface Dipole. *Appl. Phys. Lett.* **2005**, *87*, 263502.
- (27) Svane, K. L.; Hammer, B. Thermodynamic Aspects of Dehydrogenation Reactions on Noble Metal Surfaces. *J. Chem. Phys.* **2014**, *141*, 174705.